Soft Matter

PAPER

View Article Online
View Journal | View Issue

Cite this: *Soft Matter*, 2015, **11**, 1814

Wrinkling and folding of thin films by viscous stress†

Sourav Chatterjee,[a] Christina McDonald,[a] Jiani Niu,[a] Sachin S. Velankar,*[a] Peng Wang[b] and Rui Huang[b]

We examine the buckling of a thin elastic film floating on a viscous liquid layer which is itself supported on a prestretched rubber sheet. Releasing the prestretch in the rubber induces a viscous stress in the liquid, which in turn induces a compressive stress in the elastic film, leading to buckling. Unlike many previous studies on wrinkling of floating films, the buckling process in the present study is dominated by viscous effects whereas gravitational effects are negligible. An approximate shear lag model predicts the evolution of the stress profile in the unbuckled film that depends on three parameters: the rate at which the prestretch is released, the thickness of the liquid layer, and the length of the elastic film. A linear perturbation analysis is developed to predict the wavelength of wrinkles. Numerical simulations are conducted to predict nonlinear evolution of the wrinkle wavelength and amplitude. Experiments using elastic polymer films and viscous polymer liquids show trends that are qualitatively consistent with the predictions although quantitatively, the experimentally-observed wrinkle wavelengths are longer than predicted. Although this article is focused only on small-strain wrinkling behavior, we show that application of large nominal strains (on the order of 100%) leads to sharply localized folds. Thus this approach may be useful for developing buckled features with high aspect ratio on surfaces.

Received 11th November 2014
Accepted 22nd December 2014

DOI: 10.1039/c4sm02501f

www.rsc.org/softmatter

1 Introduction

Elastic instabilities of thin solid films attached to compliant substrates have attracted much attention. The most heavily-studied situation has been the compression-induced buckling of a stiff, thin elastic film bonded to a thick elastic substrate of much lower modulus. Depending on the loading conditions, a variety of buckling patterns[1,2] have been observed. The characteristic wavelength of these patterns is governed by a balance of the bending energy of the stiff film and the elastic strain energy of the substrate. Another well-studied situation is the buckling of a thin elastic film floating on a liquid surface, where the characteristic length scale is governed by a balance of the bending energy of the film and the gravitational potential of the perturbed liquid. A variation of the same situation is a liquid-bound film that is under a tensile load due to interfacial tension.[3–5] Both these situations have been exploited to measure the mechanical properties of thin films.[3,6] One of the motivations underlying this research is to measure the mechanical properties of thin films attached to highly viscous liquids, for which the previous methods[3,6] are unsuitable.

Most of the previous studies examined elastic instabilities at static equilibrium. This paper is concerned with the kinetics of wrinkling, specifically, the rate-dependent buckling instability of a liquid-supported elastic film where viscous effects are prominent. Such situations are known to arise in thin film processing of metal, polymer or inorganic materials when a thin solid film bonded to a highly viscous layer may relax a residual compressive stress by buckling out-of-plane.[7–10] Viscosity-dominated rate effects are also relevant to the analogous situation of filament buckling (rather than thin film buckling) which explains how microtubules embedded in cytoplasm provide support to cell walls.[11,12] Viscous effects in buckling are also likely to be important in the flow of suspensions of high-aspect ratio solids such as carbon nanotubes or graphene sheets since viscous drag decreases proportionally with size whereas bending stiffness decreases more rapidly with a higher power in size. Thus, at a given aspect ratio and deformation rate, a nanoscale object under viscous flow is more likely to buckle.

Numerous theoretical and computational studies on the buckling of thin films bonded to viscous liquid layers have been conducted.[13–15] Rather than an energy minimization or force balance approach used for the static buckling problem, the time-dependent buckling problem is tackled by a kinetic approach calculating the fastest-growing wavelength for the given geometry and material properties. The various situations that have been considered include elastic films that are infinite in extent,[13–15] the effect of lateral extension of the films that are

[a]*Department of Chemical Engineering, University of Pittsburgh, Pittsburgh, PA 15261, USA. E-mail: velankar@pitt.edu*

[b]*Department of Aerospace Engineering and Engineering Mechanics, University of Texas, Austin, TX 78712, USA*

† Electronic supplementary information (ESI) available. See DOI: 10.1039/c4sm02501f

finite in extent,[16] elastic films on viscoelastic liquids,[17,18] and films with anisotropic elastic properties.[19] In all of these studies, the compressive stress in the film was prescribed as an initial condition, appropriate for situations such as residual stresses arising from epitaxial growth or a mismatch in thermal expansion of the film and the viscous layer. Here we consider a more complex situation where an initially stress-free film is in contact with a viscous liquid. When the liquid is subjected to a compressive flow field, the corresponding viscous stresses developed in the liquid induce a compressive stress in the film. Unlike the prestress in the previous studies, here the buckles are generated by the viscous stresses. While carefully-controlled experiments will be described later in this paper, the basic phenomenon may be illustrated by a simple "hand experiment" shown in the Movie M1.mpg (online ESI†). A highly viscous liquid was poured onto a strip of rubber and allowed to spread into an elongated puddle. A strip of polyester film (0.001 or 0.0005 inch thick "plastic shimstock", purchased from McMaster-Carr Industrial Supply Co.) was placed on the surface. The rubber strip was then stretched by hand and released. In the first instance shown in the video, the release rate was relatively slow and little or no buckling was evident. In the second instance, the release rate was much higher, and severe buckles appeared. These buckles then relaxed by lateral extension of the film, which eventually reached a flat state again. The fact that the buckling process depends on the release rate suggests that it is induced by viscous forces, although gravitational effects could be present during the post-buckling stage. We emphasize that this situation is different from the previous cases[20] where the weight of the liquid provided a "gravitational stiffness" which determined the buckle wavelength. In those cases, the balance between bending elasticity and the gravitational potential of the liquid determines the buckle wavelength:[20] $\lambda = 2\pi\left(\frac{Eh^3}{12\rho g}\right)^{0.25}$, where ρ is the mass density of the liquid, E is the elastic modulus of the film, and h the film thickness. For the polyester film in the video, the buckle wavelength is calculated to be roughly 40 mm – several times larger than observed in the video. Incidentally, the fact that gravity is not the primary factor determining the buckles is shown unambiguously in the video: tilting the rubber strip so that the normal to the film surface is horizontal did not change the buckling behavior significantly.

The video also shows that if the rubber is stretched to a large strain and then released, the buckles become localized, reminiscent of folds.[20,21] Moreover, the surrounding air invades under the buckle from both edges of the film. In the case illustrated, the two air/liquid menisci invading from the edges do not meet under the film and a "window" of liquid persists. Although such air invasion appears visually similar to delamination from the liquid surface,[22] it is not true delamination since a layer of liquid remains adhered to the underside of the film.

The generation of tall, localized folds is potentially useful since it provides a simple route to producing high-amplitude buckles. When buckles are induced by differential thermal expansion, typical strains are on the order of 1%, thus limiting the buckle magnitude to a few percent of the wavelength. In contrast, commercial rubber sheets can be stretched reversibly well in excess of 200%. Thus, with a viscous liquid layer, this strain in the rubber can be harnessed to develop high aspect ratio features on surfaces. An example of this is illustrated in Fig. 1. Here the experimental procedure was identical to that shown in the Movie M1.mpg,† but the layer used to support the polyester film was polystyrene (PS) of low molecular weight (Piccolastic A75, Eastman Chemicals). This PS is a glassy solid at room temperature, but flows when its glass transition temperature ($\sim$35 °C) is exceeded. Accordingly, the entire system (film-on-PS-on-rubber strip) was heated to 100 °C, removed from the oven, and then immediately stretched by hand and released, analogous to the Movie M1.mpg.† The system cools rapidly during this entire stretch-and-release process, and thus the buckled structure can be quenched. If the prestretch strain is small, wrinkles of modest amplitude appear (Fig. 1a), whereas with a large prestretch, the buckles evolve into tall folds (Fig. 1d). In either case, it is possible to peel the polyester film off the surface of the vitrified PS (Fig. 1b, c & e–g), leaving the wrinkles or folds replicated on the PS layer. Incidentally, it is noteworthy that after peeling, the polyester film is left permanently wrinkled, in contrast to the corresponding experiment at room temperature (M1.mpg†) in which the film relaxed back to a flat state. This suggests that in the high temperature experiment of Fig. 1, the yield strain of the polyester film was exceeded during the buckling process. Regardless, Fig. 1 shows that by using a thermoplastic polymer as the supporting layer, a surface can be patterned with wrinkles or folds of large amplitude.

It is important to emphasize that the method of supporting the liquid layer on a rubber sheet allows the film to be subjected to compressive stress homogeneously over almost its entire length. In contrast, simply pushing on the ends of the film would – in the presence of large viscous dissipation – only induce localized compression. Incidentally, we note that this experimental procedure resembles that of Vella *et al.*[23] except that (1) there is a viscous liquid layer between the film and the rubber sheet, and (2) the compression occurs at a finite rate rather than quasi-statically.

The rest of this article examines the early stages of this process, *viz.* the initial development of buckles, analytically and experimentally. Issues such as post-buckling structural evolution at large strain, or the invasion of air under the buckles, will not be considered further here. While the chief goal of this paper is to expand knowledge of dissipative effects in thin film buckling phenomena, we mention two practical motivations for our research. The first is to develop methods that can generate high amplitude buckles, as was already discussed in Fig. 1 above. Additionally, we are motivated by the desire to measure the mechanical properties of reactive compatibilizer films, which are thin films that form at the interface between immiscible polymers.[24,25] These films, which are roughly one macromolecule thick, are often crosslinked and hence solid-like,[26] but there is no method at present to measure their mechanical properties. Past research has shown how the

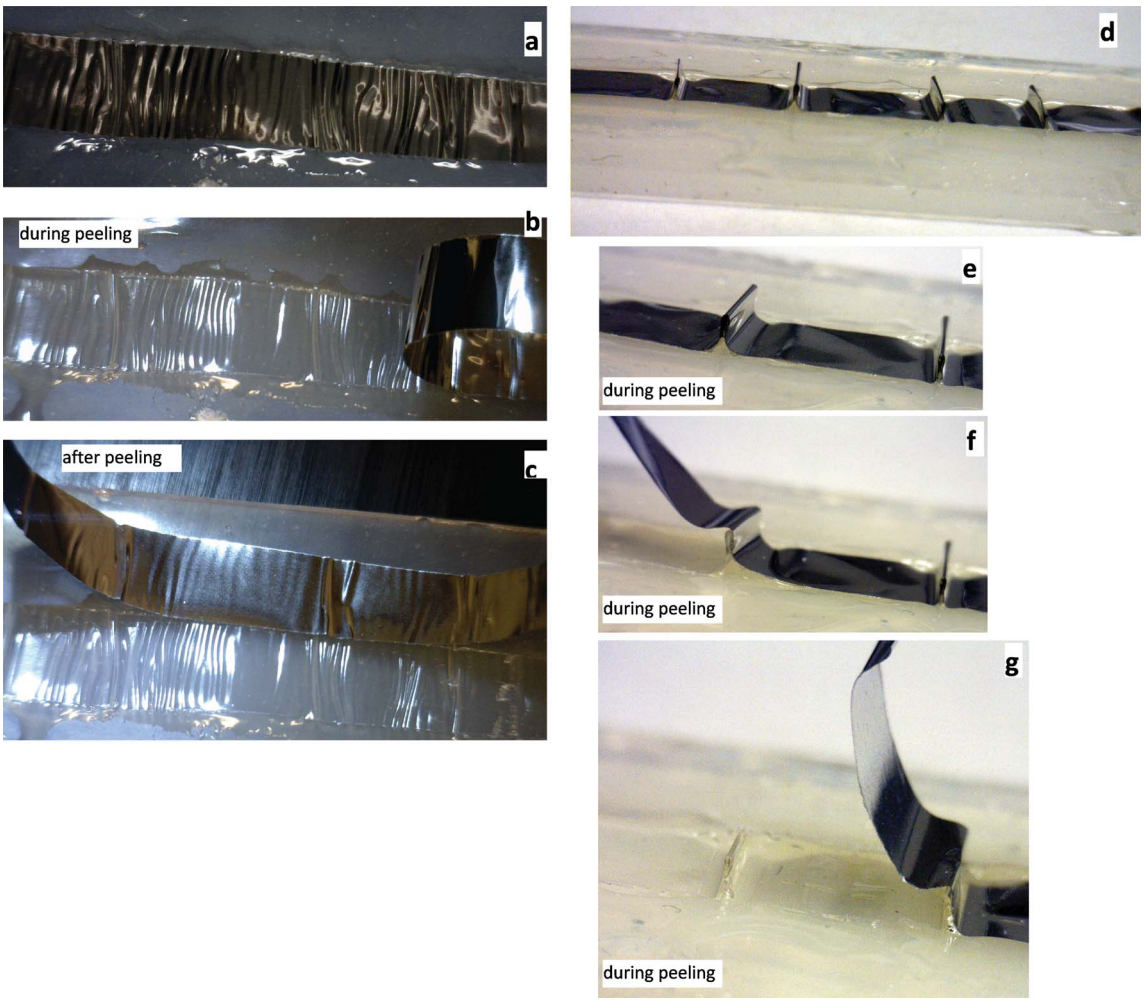

Fig. 1 Wrinkles can be quenched using a liquid that can be solidified by cooling. (a and d) correspond to small or large prestretching of the rubber, respectively. The film can subsequently be peeled off, leaving the wrinkle or fold pattern imprinted on the surface of the vitrified polystyrene. (b, e–g) show the process during peeling, whereas (c) shows the peeled film and the vitrified polystyrene laid side-by-side.

equilibrium buckling of thin films on compliant supports can be used to estimate the mechanical properties of the films.[3,6] However, those methods cannot be applied to reactive compatibilizers since the bulk liquids have high viscosity (10^5 Pa s is typical for molten polymers), and it is not possible to deform sufficiently slowly to maintain mechanical equilibrium. The method developed here (with the compatibilizer film sandwiched between two molten polymer layers rather than floating at the air/polymer surface) offers the possibility of measuring compatibilizer mechanical properties.

The remainder of this paper is organized as follows. In Section 2, we use an analytical shear-lag model to predict the evolution of the compressive stress profile in the film prior to buckling, which allows a qualitative comment on the critical condition and the buckle wavelength. Section 3 performs a linear perturbation analysis of the solution from Section 2 to predict the wavelength at which buckles grow the fastest. Section 4 describes experiments which are compared against these predictions. Section 5 presents numerical simulations and discussions.

2 Analytical model

2.1. Governing equations

The geometry and coordinate system for the model is shown in Fig. 2a & b. We assume the film to be a thin elastic plate. The analysis is similar to that of Huang and Suo[13] who studied wrinkling of a pre-compressed film on a viscous layer. However, it differs from Huang and Suo[13] in two ways. First, the lower surface of the viscous layer is not stationary in the present case, but instead subject to a specified strain rate due to contraction of the rubber sheet. Second, the film does not bear a prestress; instead, the compressive stress in the film develops with time. Thus, the buckling instability is driven not by relaxation of the pre-stressed film, but by the viscous stresses transferred from the contracting rubber sheet to the film *via* the liquid layer.

As in Huang and Suo,[13] the analysis requires solving the coupled equations describing the elastic deformation of the film and the viscous flow of the liquid layer. The various parameters can be non-dimensionalized using the film thickness h as the length scale, $\frac{\eta(1-\nu^2)}{E}$ as the time scale, and $\frac{E}{1-\nu^2}$

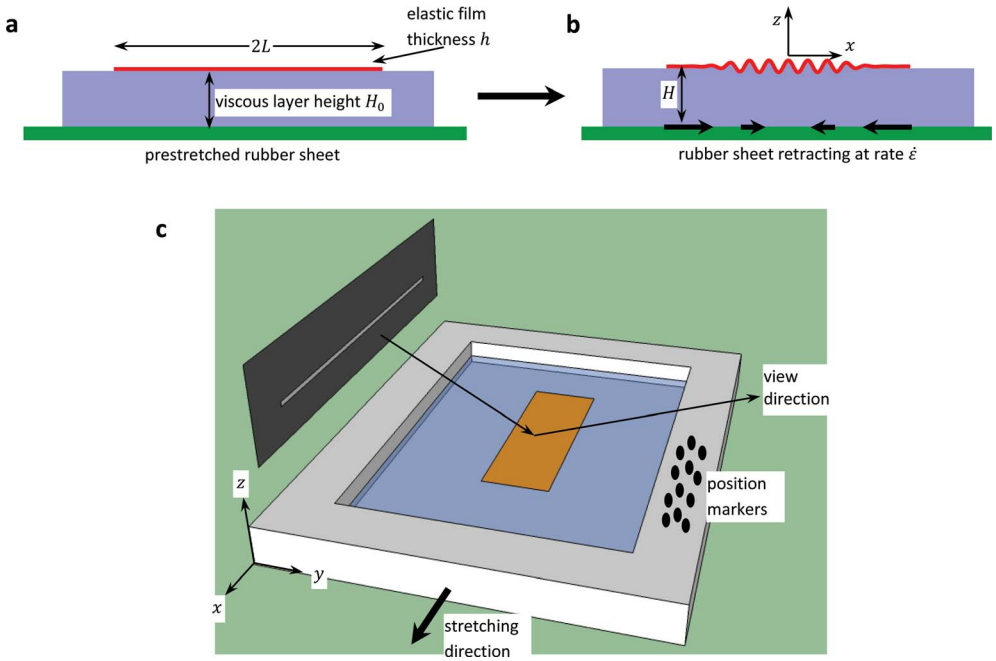

Fig. 2 (a) An initially flat film floating on a fluid layer, covering a prestretched rubber sheet. (b) The film wrinkles when the rubber sheet is unstretched at a controlled rate. (c) Schematic of experimental setup.

as the stress scale. Thus, the scaled parameters are: $x_s = \frac{x}{h}$, $t_s = \frac{tE}{\eta(1-\nu^2)}$, $H_s = \frac{H}{h}$, $L_s = \frac{L}{h}$, $u_s = \frac{u}{h}$, $w_s = \frac{w}{h}$, $\sigma_s = \frac{\sigma(1-\nu^2)}{E}$, $T_s = \frac{T(1-\nu^2)}{E}$, and $p_s = \frac{p(1-\nu^2)}{E}$. Here u and w are the in-plane and out-of-plane displacements, p, σ and T respectively refer to the pressure, compressive stress and shear stress on the film, E and ν are Young's modulus and Poisson's ratio of the film, and η is the viscosity of the liquid. With these scaled parameters, the evolution equations for the in-plane and out-of-plane displacements can be written as (see online ESI for details†):

$$\frac{\partial w_s}{\partial t_s} = \frac{\partial}{\partial x_s}\left(\frac{{H_s}^3}{3}\frac{\partial p_s}{\partial x_s} - \frac{{H_s}^2}{2}T_s - \beta H_s x_s\right) \quad (1)$$

$$\frac{\partial u_s}{\partial t_s} = -\frac{{H_s}^2}{2}\frac{\partial p_s}{\partial x_s} + H_s T_s + \beta x_s \quad (2)$$

where $\beta = (1-\nu^2)\eta\dot{\varepsilon}/E$ is the normalized strain rate. The non-dimensional boundary conditions to be applied at $x_s = \pm L_s$ are:

No normal stress:

$$\frac{\partial u_s}{\partial x_s} + \frac{1}{2}\left(\frac{\partial w_s}{\partial x_s}\right)^2 = 0 \quad (3)$$

No bending moment:

$$\frac{\partial^2 w_s}{\partial {x_s}^2} = 0 \quad (4)$$

No shear force:

$$\frac{\partial^3 w_s}{\partial {x_s}^3} = 0 \quad (5)$$

No pressure:

$$\frac{1}{12}\frac{\partial^4 w_s}{\partial {x_s}^4} - T_s\frac{\partial w_s}{\partial x_s} = 0 \quad (6)$$

2.2. Shear lag solution

The coupled nonlinear equations can be solved numerically (Section 5). As an approximation, we present an analytical shear-lag solution by ignoring the variation of the fluid pressure and setting

$$\frac{\partial p}{\partial x} = 0 \quad (7)$$

As a result, the flow velocity of the liquid varies linearly from the bottom surface to the top surface (ESI eqn (S5)†). Further, we neglect all the nonlinear terms in the governing equations. With these simplifications, and inserting online ESI eqn (S11) and (S12)† into eqn (2), we get:

$$\frac{\partial u_s}{\partial t_s} = H_{s0}\frac{\partial^2 u_s}{\partial {x_s}^2} + \beta x_s \quad (8)$$

which takes the form of a linear diffusion equation with a dimensionless diffusivity H_{s0} and a source term βx_s. In effect, the last term in the preceding equation seeks to generate a linearly-varying displacement (and hence a constant strain)

throughout the length of the film, whereas the first term on the right hand side seeks to diffusively redistribute the strain to be consistent with the boundary conditions (zero normal stress at the film ends).

With the initial condition, $u_s(x_s,0) = 0$, and the boundary condition, $\left.\frac{\partial u_s}{\partial x_s}\right|_{x_s=\pm L_s} = 0$, the solution to the diffusion equation is:

$$u_s(x_s,t_s) = \frac{\beta {L_s}^2}{2H_{s0}}\left(x_s - \frac{{x_s}^3}{3{L_s}^2}\right) + \sum_{m=1}^{\infty} A_m \sin(b_m x_s)\exp\left(-{b_m}^2 H_{s0} t_s\right) \tag{9}$$

where $b_m = \frac{(2m-1)\pi}{2L_s}$ and $A_m = \frac{(-1)^m}{(2m-1)^4}\frac{32\beta {L_s}^3}{\pi^4 H_{s0}}$.

The scaled normal stress σ_s in the elastic film is then obtained as:

$$\sigma_s(x_s,t_s) = \frac{\beta {L_s}^2}{2H_{s0}}\left(1 - \frac{{x_s}^2}{{L_s}^2}\right) + \sum_{m=1}^{\infty} A_m b_m \cos(b_m x_s)\exp\left(-{b_m}^2 H_{s0} t_s\right) \tag{10}$$

It is noteworthy that the scaled normal stress σ_s has a direct physical significance: σ_s is actually the in-plane compressive strain in the film. The corresponding dimensionless shear stress at the interface is obtained from ESI eqn (S12):†

$$T_s(x_s,t_s) = -\frac{\beta x_s}{H_{s0}} - \sum_{m=1}^{\infty} A_m {b_m}^2 \sin(b_m x_s)\exp\left(-{b_m}^2 H_{s0} t_s\right) \tag{11}$$

Finally, the scaled out-of-plane displacement w_s, can be obtained from eqn (1). By neglecting the nonlinear terms and the pressure gradient, we have:

$$\frac{\partial w_s}{\partial t_s} = -\frac{{H_{s0}}^2}{2}\frac{\partial T_s}{\partial x_s} - \beta H_{s0} \tag{12}$$

With eqn (11), we obtain:

$$w_s(x_s,t_s) = -\frac{1}{2}H_{s0}\beta t_s + \frac{1}{2}H_{s0}\sum_{m=1}^{\infty} A_m b_m \cos(b_m x_s) \times \left[1 - \exp\left(-{b_m}^2 H_{s0} t_s\right)\right] \tag{13}$$

Eqn (9)–(11), and (13) together represent the time-dependent shear lag solution of the problem. These four quantities are plotted in Fig. 3 for a specific set of parameters. These parameters were selected to be the same as those for one of the experiments (Fig. 8) discussed later.

The shear-lag solution consists of a time-dependent infinite series and a steady-state solution. A dimensionless diffusion time scale can be defined for the "slowest" term in the infinite series:

$$\tau_s = \frac{1}{H_{s0}{b_1}^2} = \frac{4L^2}{\pi^2 h H_0} \tag{14}$$

which is purely a geometric quantity. The corresponding dimensional diffusion time is:

$$\tau = \tau_s\frac{\eta(1-\nu^2)}{E} = \frac{4L^2}{\pi^2 h H_0}\frac{\eta(1-\nu^2)}{E} \tag{15}$$

We can identify two limits of the shear-lag solution. First, in the short time limit with $t_s \to 0$, the in-plane displacement is almost linear with x_s (Fig. 3a), and the out-of-plane displacement is nearly constant (Fig. 3b). Furthermore, except for a narrow region near the ends of the film, the in-plane normal stress (Fig. 3c) is nearly constant and negative (*i.e.* compressive), and the shear traction is nearly zero (Fig. 3d).

With increasing time, the solution approaches a steady state when $t_s \gg \tau_s$ or equivalently $t \gg \tau$. In the steady state, the elastic film is subjected to a linearly distributed interfacial shear traction, T_s, and correspondingly, a quadratic distribution of the normal stress, σ_s. Meanwhile, the steady-state flow velocity of the liquid varies linearly from zero at the top surface to the velocity of the retracting rubber sheet at the bottom. The flow rate varies linearly with x, leading to a rigid-body motion of the film with a constant rate for the out-of-plane displacement, w_s. As seen from eqn (13), in the steady state ($t \to \infty$), we have

$$w_s(x_s, t_s \to \infty) = -\frac{1}{2}H_{s0}\beta t_s + \frac{1}{2}H_{s0}\sum_{m=1}^{\infty} A_m b_m \cos(b_m x_s) \tag{16}$$

where the first part on the right-hand side is the uniform (*i.e.* position-independent) rise of the film with time, and the second part captures the steady-state deflection profile of the film.

The quantity most relevant to understanding the buckling behavior is the compressive stress in the film, eqn (10). This stress is always highest at the center ($x_s = 0$):

$$\sigma_s(x_s = 0, t_s) = \frac{\beta {L_s}^2}{2H_{s0}} + \sum_{m=1}^{\infty} A_m b_m \exp\left(-{b_m}^2 H_{s0} t_s\right) \tag{17}$$

The first term on the right hand side is the maximum possible value of σ_s which is reached at the center ($x_s = 0$) in the steady state ($t \to \infty$):

$$\sigma_s^{\max} = \frac{\beta {L_s}^2}{2H_{s0}} \tag{18}$$

Fig. 4a illustrates the time-evolution of the scaled normal stress at the center given by eqn (17). Regardless of the geometry or rate, the scaled normal stress rises from zero to $\sigma_s^{\max}$ over a dimensionless timescale proportional to τ_s. As such, the dependence of the stress evolution on the experimentally-controllable parameters (liquid thickness, film length, and strain rate) is fully captured by the two dimensionless parameters, τ_s and $\sigma_s^{\max}$. Fig. 4b illustrates the effect of the three experimentally-controllable parameters on the time-evolution. In particular, the scaled compressive stress at any instant increases with increasing film length (L_s) or increasing rate, or decreasing liquid layer thickness (H_{s0}).

The development of the compressive normal stress in the elastic film is the driving force for the wrinkling instability. Kinetically constrained by the viscous layer, the growth of wrinkles depends on the stress magnitude. As predicted by

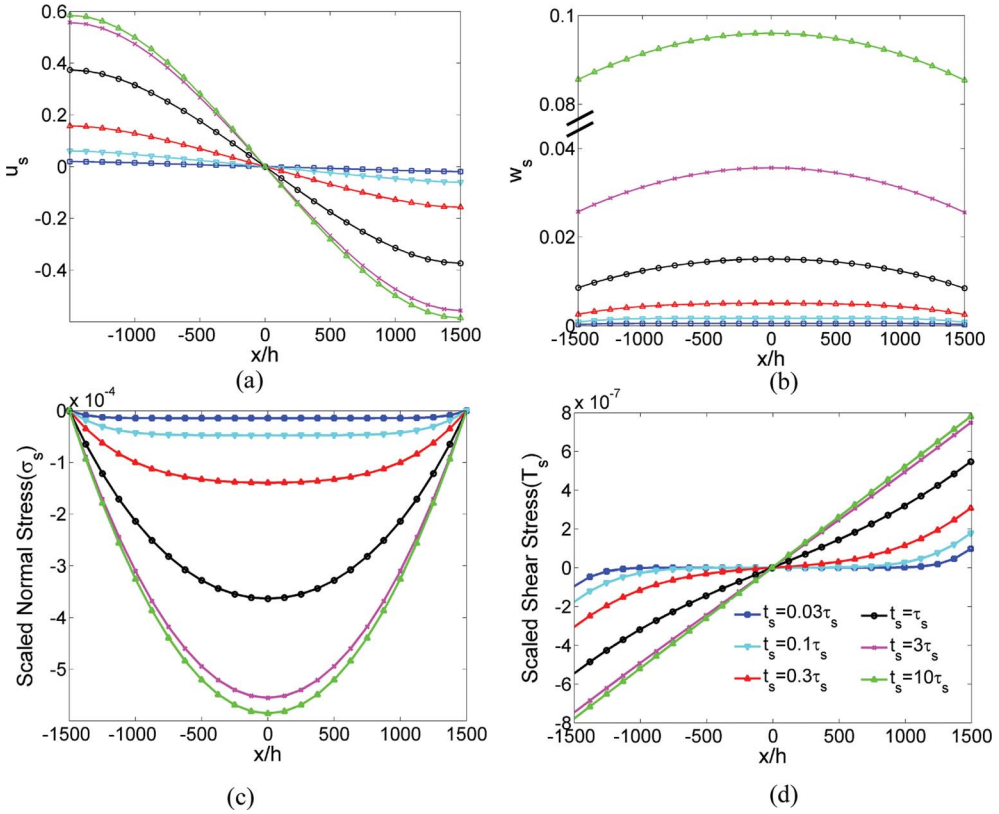

Fig. 3 Values of (a) in-plane and (b) out-of-plane displacements, (c) scaled normal stress, and (d) scaled shear stress obtained from the shear lag solution at various times. The geometric parameters used are: film length $2L = 75$ mm, film thickness $h = 0.025$ mm, liquid layer thickness $H_0 = 0.9$ mm, $\dot{\varepsilon} = -0.088\ s^{-1}$. The material parameters are: modulus $E = 5$ GPa, viscosity $\eta = 1170$ Pa s, and Poisson's ratio $\nu = 0.3$. The corresponding dimensionless parameters are $L_s = 1500$; $H_{s0} = 36$; $\beta = -1.87 \times 10^{-8}$. Eqn (14) and (15) give $\tau_s = 25\,330$ and $\tau = 0.00539$ s.

Huang and Suo[14] for an infinitely long film subject to a uniform prestress, the wavelength of the fastest-growing wrinkles decreases with increasing prestress magnitude, and the growth rate of the wrinkle amplitude increases with increasing prestress magnitude. For a finite thin film, the compressive stress is typically non-uniform, high around the center and low near the ends. Qualitatively, wrinkles may be expected to grow near the center with relatively short wavelength. Near the ends, the film remains relatively flat since the wrinkles grow slowly and the wrinkle wavelength is expected to be long.

Since wrinkle wavelengths exceeding the film length are difficult to identify experimentally, a critical stress magnitude for seeing any wrinkles at all may be estimated based on the classical Euler buckling solution with a scaled critical stress: $\sigma_s^{cr} = \frac{\pi^2}{3{L_s}^2}$. A critical condition for buckling by the viscous stress may be estimated by setting the magnitude of the maximum compressive stress in the steady state (eqn (18)) to exceed the critical stress, *i.e.*, $|\sigma_s^{max}| \geq \sigma_s^{cr}$, leading to

$$|\beta| \geq \frac{2\pi^2 H_{s0}}{3{L_s}^4} \tag{19}$$

where the absolute value of β is taken because β is negative for compression. Given specific geometric parameters L_s and H_{s0}, this condition predicts a minimum dimensionless strain rate necessary to induce buckling by the viscous stress. Using typical experimental values ($L_s = 1500$; $H_{s0} = 36$, same as in Fig. 8 below), $|\beta| \geq 4.7 \times 10^{-11}$ is obtained, which is over 100-fold lower than typical experimental values. Furthermore, this minimum compression rate has a very strong (power -4) dependence on length. This will be tested experimentally. It must be emphasized that this minimum compression rate is a lower bound estimate since the compressive stress over much of the film is lower than σ_s^{max}.

Finally, according to the Euler buckling model, buckles of the shortest wavelength that can be sustained in the film may be expected to scale inversely with the compressive stress, $\lambda_{min} \sim |\sigma_s^{max}|^{-0.5}$. Accordingly, eqn (18) suggests that the wrinkle wavelength is expected to scale as $\left(\frac{{L_s}^2|\beta|}{H_{s0}}\right)^{-0.5}$, or equivalently, the wave number scales as $\left(\frac{{L_s}^2|\beta|}{H_{s0}}\right)^{0.5}$. This prediction will be tested experimentally.

3 Approximate linear perturbation analysis

The shear lag solution to the coupled solid–liquid problem assumes that the film does not buckle although a deflection

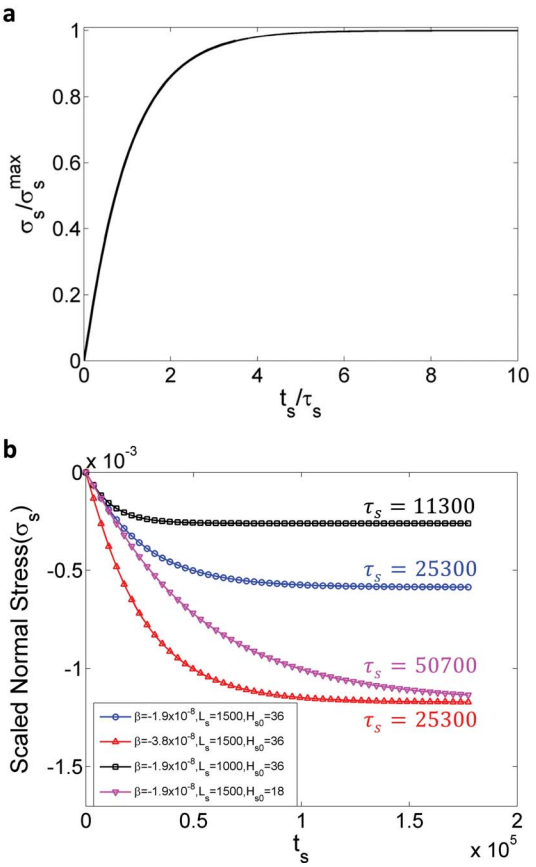

Fig. 4 (a) Evolution of the scaled normal stress at the center of the film (normalized by the long-time value) with scaled time (normalized by τ_s). In this normalized form, the evolution is independent of all physical parameters. (b) Scaled normal stress at the center of the film as a function of scaled time, for various lengths and applied strain rates. The open blue circles refer to the same parameters as Fig. 3. The other curves change one dimensionless parameter as indicated in the legend.

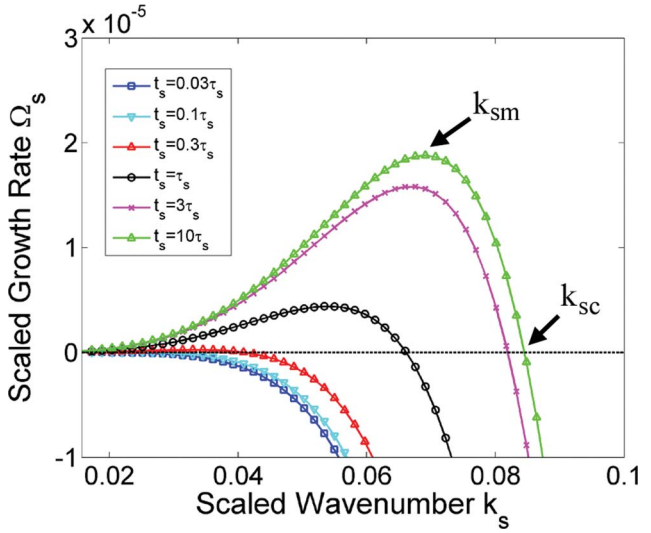

Fig. 5 Scaled growth rate as a function of scaled wave number at the center of the film, obtained at different times during compression. All geometric and material parameters are identical to Fig. 3.

profile is predicted as a result of mass conservation in the underlying liquid. However, the induced compressive stress in the film could cause buckling instability, deviating from the shear-lag solution. The stability of the shear-lag solution can be tested by a linear perturbation analysis assuming an out-of-plane displacement in the form of:

$$w_s^p = B_0\, e^{\Omega_s t_s + i k_s x_s} \tag{20}$$

and a corresponding out-of-phase perturbation to the in-plane displacement:

$$u_s^p = A_0\, e^{\Omega_s t_s + i\left(k_s x_s + \frac{\pi}{2}\right)} \tag{21}$$

where A_0 and B_0 are small initial amplitudes, $k_s = kh$ is the non-dimensional wave number of the perturbation, and Ω_s is a non-dimensional complex growth rate of the perturbation. The function $\Omega_s(k_s)$ is dubbed the "dispersion relation" henceforth in this paper. This approach is an approximate one because the non-dimensional growth rate Ω_s is taken to be independent of position and time. In reality, since the stress distribution is non-uniform, Ω_s depends on x_s. Nevertheless, near the center of the film, this approximation is reasonable, and allows comparison with experiments. Moreover at short times ($t_s \ll \tau_s$), this approximation is strictly valid over most of the film because the stress is independent of position except in a zone near the ends (Fig. 3c).

As detailed in the online ESI,† the linear perturbation analysis can be represented in the form of an eigenvalue problem. The solution of this eigenvalue problem gives the instantaneous growth rate Ω_s. Fig. 5 shows Ω_s as a function of the normalized wave number for the same set of parameters as used in Fig. 3, and at the same times as used in Fig. 3. Not surprisingly, the dispersion relation $\Omega_s(k_s)$ changes with time until $t_s \sim 10\tau_s$, and then becomes nearly invariant with time. This is because for $t_s \gg \tau_s$, the only change in shear lag solution with time is the steady-state spatially-uniform increase in the out-of-plane deflection, which has only a weak effect on the dispersion relation.

At short times, all wave numbers except those close to zero are stable, *i.e.* have negative growth rate, since the scaled compressive stress, σ_s, is small. As σ_s increases with time as per Fig. 4, the growth rate becomes positive for k_s values smaller than a critical value denoted k_{sc}, with the fastest growth occurring at a scaled wave number denoted k_{sm}. The values of k_{sc} and k_{sm} both increase with time until, for $t_s \gg \tau_s$, they reach time-invariant steady-state values.

It is useful to compare the situation at hand with the previously-studied case of a film with an initial prestrain resting on a quiescent liquid layer. In that case, the dispersion relation depends on two parameters, the prestrain ε_0, and the liquid layer height H_{s0}.[14] As a first approximation, the current situation may be regarded as analogous, with ε_0 being taken as the instantaneous value of σ_s. This analogy then permits an estimation of the instantaneous dispersion relation simply from the dispersion relation for the prestrained film.[14] Fig. 6 shows

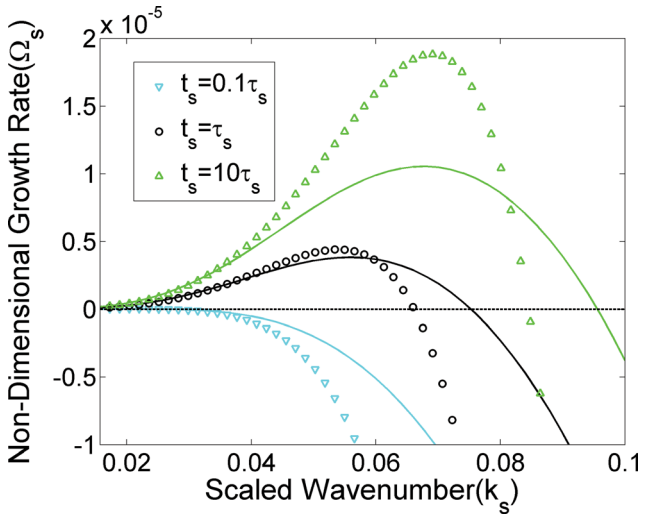

Fig. 6 Dispersion relation at three specific times compared with the dispersion relation from ref. 14 using the instantaneous value of σ_s as the prestrain.

that this analogy is somewhat reasonable: the critical and maximally-growing wave numbers are in reasonable agreement for the two situations, whereas the growth rate is higher for the situation examined in this paper.

We now turn to the dependence of the wrinkling instability on the compression rate and the liquid layer thickness. Fig. 7a shows that fastest-growing wave number, k_{sm}, increases with increasing compressive strain rate, $|\beta|$. It is noteworthy that at long times, the rate dependence agrees reasonably with the scaling, $k_{sm} \propto |\beta|^{0.5}$ (the best fit exponent is 0.52 rather than 0.5), which was anticipated from a stress argument at the end of Section 2.2.

Fig. 7b shows that the fastest growing wave number reduces with increasing liquid layer thickness. At long times, the dependence follows the scaling, $k_{sm} \propto {H_{s0}}^{-0.5}$, in accordance with the qualitative stress argument in Section 2.2. However at short times, k_{sm} is almost independent of the liquid layer thickness. The shear lag model provides a qualitative explanation for this result. At short times, eqn (17) can be expanded as a Taylor series to obtain

$$\sigma_s(x_s = 0, t_s \ll \tau_s) = -H_{s0} t_s \sum A_m {b_m}^3 \cos(b_m x_s) = \beta_s t_s = \dot{\varepsilon} t \quad (22)$$

which is independent of the liquid thickness. Thus, at short times, the scaled normal stress near the center of the film is simply the strain applied by the rubber sheet – increasing with time but otherwise independent of any geometric parameters. As a result, the fastest-growing wave number k_{sm} is also independent of H_{s0} at the short-time limit.

4 Experimental

4.1. Materials and experimental procedure

Fig. 2c shows a schematic of the experimental setup. A polymeric film is floated on a highly viscous layer, which is contained in a stretchable elastomeric tray. The rectangular tray (141 mm × 105 mm) is made out of silicone rubber (GI-245, Silicone Inc.), and is capable of large reversible elongation. The tray is mounted on a trolley-rail system, with the bottom of the tray leveled. One end of the tray is attached to a linear DC actuator. A weighed quantity of polyisoprene (molecular weight ~46 kg mol^{-1}; Kuraray Chemicals; $\eta = 1170$ Pa s) is poured into the tray and allowed to stay quiescent for 15–20 hours to ensure that the surface of the liquid layer is horizontal. The liquid layer thickness is controlled *via* the volume of the liquid poured into the tray, ranging from 0.9 mm to 2.5 mm.

The films are polyester "shimstock" (McMaster-Carr Industrial Supply Co.) with an elastic modulus (measured in uniaxial tension) of $E = 5$ GPa. These films are sold commercially for use as spacers of precise thickness, and hence are available inexpensively in the form of large sheets which can be cut to desired size. In all experiments discussed here, the film thickness is 25 μm (nominal 0.001 inch). Limited experiments at lower film thickness were also conducted but these films had some pre-existing wrinkles and hence are not discussed here.[27] Films were cut into rectangles of 25 mm width and lengths ranging from 50 to 80 mm. Each rectangular film was then laid down slowly on the liquid surface in an "unpeeling" manner using a manual translation stage. This procedure guarantees that bubbles do not get trapped under the film, and also minimizes damage to the film. The film was allowed to float quiescently on the liquid surface overnight before further experiments.

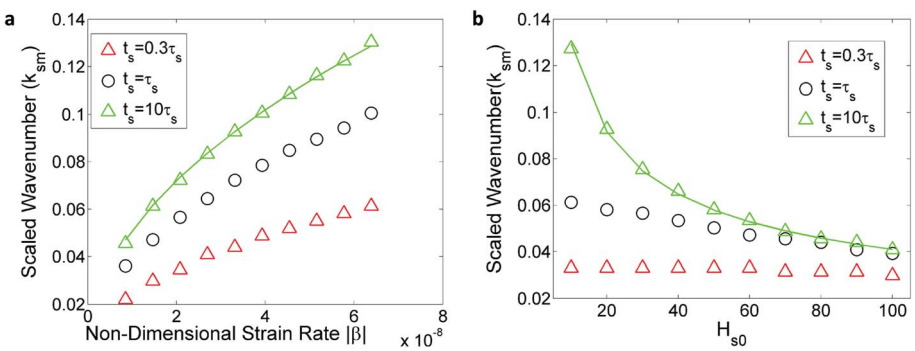

Fig. 7 Fastest growing wave numbers as a function of (a) applied non-dimensional strain rate $|\beta|$ and (b) substrate thickness at various times. All parameters are identical to those in Fig. 3, except that β is varied in (a), and H_{s0} is varied in (b). Solid lines are fits to the green triangles with a dependence of $|\beta|^{0.5}$ and ${H_{s0}}^{-0.5}$ respectively.

In each experiment, the linear stage was actuated at a slow speed so as to stretch the tray by roughly 15% as compared to its relaxed length. Note that after this stretching, the liquid layer thickness must be slightly smaller than the original value, but for the strains involved, this effect is negligible. After ~2 minute waiting time, the stage was actuated in the opposite direction at a fixed voltage (which controls the speed) to permit retraction of the tray, and buckles of the film were monitored. The retraction was stopped after about 7% contraction. Note that the retraction was stopped before the tray recovered its fully-relaxed length because the rate of recovery would slow down considerably if the tray were allowed to approach its fully-relaxed length. The tray deformation and film profile were recorded at 30 frames per s using a camcorder (Panasonic SDR-70). The Movie file M2.mpg† shows a video of the entire process.

The wrinkle wavelength was of the order of a few millimeters, and hence wrinkles can be observed directly on the film. However, direct visual observation has relatively poor sensitivity to small amplitude wrinkles. Accordingly, the video was recorded so as to capture the image of a white line drawn on paper and reflected off the surface of the film (see Fig. 2c). This reflection is far more sensitive for detecting height variations in the film. It must be emphasized however, that the reflected line is severely distorted optically and does not represent the actual wrinkle amplitude. In fact the wrinkle amplitude, which can be judged qualitatively by examining the edge of the film, *e.g.* in Fig. 8d, remains modest throughout this process.

Experiments under one set of parameters (0.9 mm liquid layer thickness, 75 mm film length) were repeated several times. The degree of reproducibility in three of those experiments is illustrated in online ESI Fig. S1† (discussed in detail in Section 4.4 below). Limited repeat experiments were also conducted at other liquid thicknesses or film lengths and showed similar reproducibility, however under conditions of weak buckling (small $\dot{\varepsilon}$, large H_0) it is more difficult to quantify wavelengths due to the small amplitude and large wavelength of buckles.

4.2. Determination of strain and strain rate

Typical frames extracted from videos such as M2.mpg† are shown in Fig. 8a–f. The strain rate applied is quantified as follows. The displacement field is calculated by using digital image correlation (DIC) analysis of ink marks placed on the front edge of the tray. Fig. 8g illustrates the displacement of the markers with time, and the slope of each displacement profile yields the instantaneous strain experienced by the edge of the

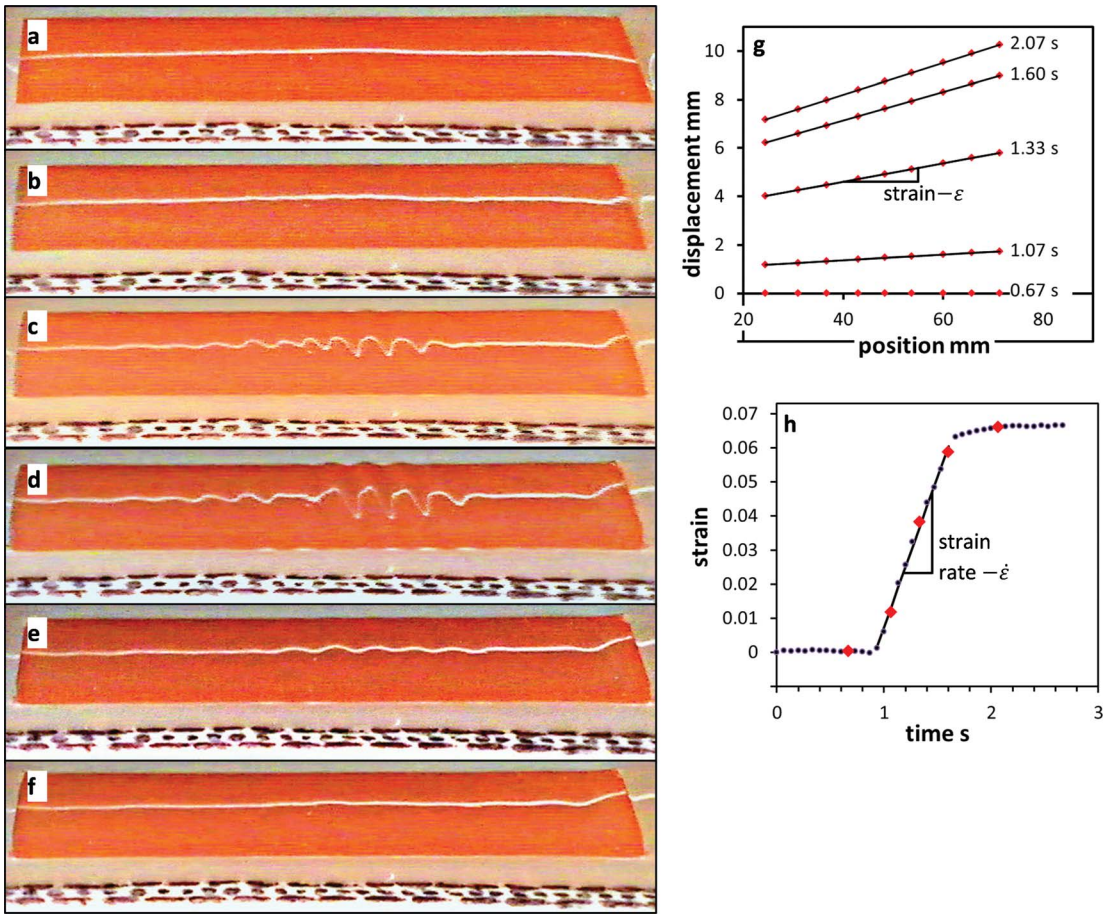

Fig. 8 Images of the film at various stages of the wrinkling process. All parameters are the same as Fig. 3. (a) initially flat film, (b–d) during compression, (e and f) relaxation phase. The white line in all images is the reflection of a white line in the background; see text. (g) Displacement profiles of ink markers in the images at the various times listed gives the strain. (h) Strains from (g) *vs.* time.

tray. Experiments with the camera placed at normal incidence, and conducted without placing the film on the liquid surface confirm that the strain profile at the edge is identical to the strain along the centerline of the tray.

Fig. 8h shows the strain as a function of time. The slight variability of the strain before the start of the retraction (*i.e.* when strain must be zero) is a measure of the uncertainty of the DIC method. During the retraction phase, the strain increases almost linearly with time, and the strain rate is taken as the magnitude of $\dot{\varepsilon}$ (a negative sign is assigned for compression, consistent with the analytical section of this paper).

4.3. Qualitative discussion of results

We will now discuss Fig. 8 in detail. This corresponds to a film with length $2L = 75$ mm and thickness $h = 0.025$ mm on a liquid layer with thickness $H_0 = 0.9$ mm. The strain rate extracted from the video is $\dot{\varepsilon} = -0.088\ \mathrm{s}^{-1}$. A video of the same process is available as online ESI.† The dimensionless parameters for this film are: $H_{s0} = H_0/h = 36$; $L_s = L/h = 1500$, and $\beta = -1.87 \times 10^{-8}$. The scaled maximum normal stress predicted by the shear-lag model is $\sigma_s^{max} = -5.9 \times 10^{-4}$. The non-dimensional timescale is $\tau_s = 25\,300$, and the corresponding dimensional time $\tau = 5.39 \times 10^{-3}$ s. It is noteworthy that the entire process of Fig. 8 occurs over a timescale far greater than τ. This points to an experimental limitation: the time-resolution of 0.033 s (*i.e.* video rate of 30 frames per s) is already far larger than τ. Hence the experimental observation is limited to the long-time behavior ($t_s \gg \tau_s$).

In the first 2–3 frames of the video, the reflection of the line does not appear substantially distorted. It is difficult to identify precisely when the buckles appear (critical strains will be discussed below), but by a strain of about 0.01 (Fig. 8b) small distortions are evident in the reflection of the white line over much of the film. With increasing compression, the buckles near the middle sharply increase in amplitude, whereas those near the ends remain small. Nevertheless, there does not appear to be a significant variation in the buckle wavelength across the length of the film. Furthermore, the videos do not allow a clear judgment of whether the buckle wavelength changes with time. Yet, both the preceding sentences regarding wavelength require a caveat: typical buckles are ~30–40 pixels wide and therefore any variation in buckle wavelength of less than 10% (corresponding to 3 pixels) cannot be measured reliably.

Incidentally we note that the reflected white line in the images distinctly suggests that the ends of the film rise

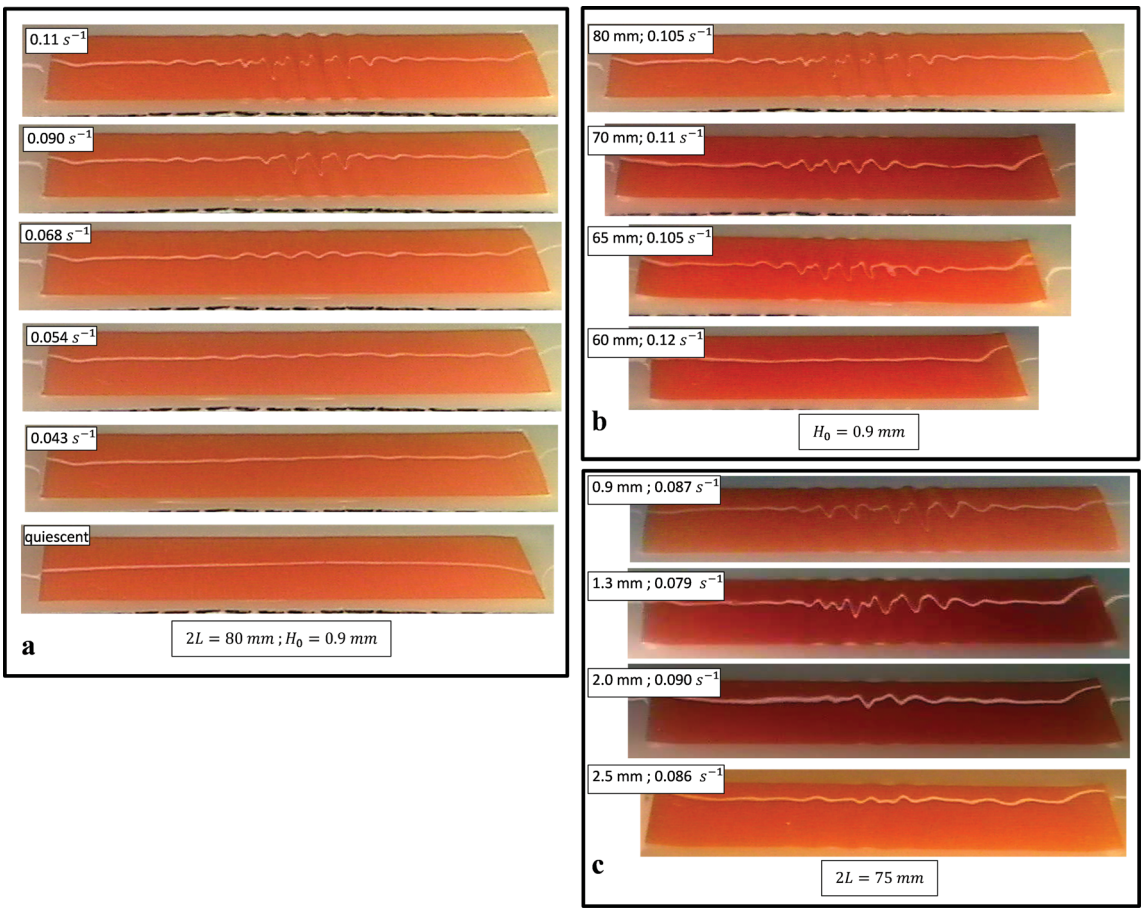

Fig. 9 Effect of each of the three parameters, $\dot{\varepsilon}$, L and H_0 on buckling. (a) $\dot{\varepsilon}$ varied at fixed L and H_0. (b) L varied at fixed H_0, while $\dot{\varepsilon}$ is roughly constant. (c) H_0 is varied at constant L while $\dot{\varepsilon}$ is roughly constant. Note that in (b) and (c), the compression rate is not exactly constant because of variations in the speed realized by the actuator.

upwards. That the front edge of the film does not appear visibly raised suggests that the upward displacement is small. Moreover the left end does not appear to rise upwards, but this is an optical artifact of the camera position. Images of a test film resting on a solid substrate with raised ends shows that the appearance changes with the camera position. This upward displacement of the ends is opposite of that predicted by the shear lag model (Fig. 3b). However this discrepancy is attributable to the fact that the shear lag model does not impose the full boundary conditions for the vertical displacement w. Numerical solutions that impose the full boundary conditions (eqn (3)–(6)) do indeed show an upward displacement of the ends, as will be discussed in Section 5.

After cessation of the strain, the film relaxes (Fig. 8e and f), with the wrinkles nearer to the ends relaxing before those near the center. This process is similar to that elucidated by Liang *et al.*[16] who showed a diffusive relaxation proceeding from the edge of the film as a result of in-plane expansion of the film. We will not consider the relaxation behavior in this paper.

Experiments were conducted across a range of compression rates, film lengths, and liquid layer thicknesses. Fig. 9 illustrates the typical buckled structures as each of these variables is changed in turn, keeping the other two fixed (at least approximately; see caption to Fig. 9). It is evident that with a decrease in rate, a decrease in film length, or an increase in liquid layer thickness, the wrinkle-amplitude reduces until wrinkles cannot be seen any more. This may be interpreted in at least two ways. First, as illustrated by the shear lag model, in the absence of buckling, there is a certain maximum compressive stress experienced by the film. If this stress is insufficient to sustain buckles at a wavelength comparable to the film length, buckling cannot happen. A second way to understand this is to recognize that the film can relax by expanding outwards.[16] If the compressive stress cannot build up sufficiently rapidly, the film will remain relaxed and flat.

4.4. Quantitative analysis

Three quantities were extracted from images taken from videos: the minimum compression rate required to induce visible buckles, the critical strain for buckling, and the wavelength of the buckles. These will each be discussed in turn.

Determining the minimum compression rate necessary for buckling requires some qualitative judgment about whether sufficient distortion is evident in the reflected image of the white line. Although there may be some ambiguity from one observer to another, the distinction can be made consistently, and hence it is possible to identify bounds for the highest strain rate that does not show buckles, and the lowest strain rate that does show buckles. These results are shown in Fig. 10. They are in reasonable agreement with the scaling, $\dot{\varepsilon} \propto L^{-4}$ (the straight line) predicted by the stress argument (eqn (19)). Incidentally, a limited set of experiments (not shown) conducted at 12.5 μm film thickness also showed a minimum rate with similar scaling dependence on the film length.

We also sought to determine critical strains from the data. In this context, the critical strain refers not to the strain in the film

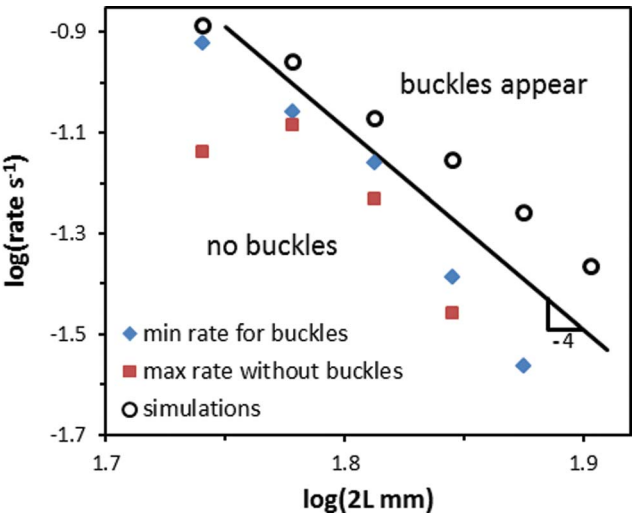

Fig. 10 Conditions for developing buckles. Buckles develop above the blue points but not below the red points. Solid line has slope of −4. Open circles are the critical strain rate from numerical simulations.

(which cannot be measured in our experiment) but the strain in the rubber sheet at the instant when buckles appear. Unfortunately, determining *when* buckles appear is subject to far more ambiguity than simply *whether* they appear (Fig. 10). Nevertheless, there is no doubt that in all the experiments, the strains at which buckles became visible far-exceeds 0.005 – indeed to our best judgment, most cases exceeded a strain of 0.01. These values are at least 10-fold larger than the value of $\sigma_s^{max} = 5.9 \times 10^{-4}$ calculated from shear lag model. This is consistent with the fact that the timescale of buckling far exceeds the diffusion time scale τ needed to reach the steady state. Thus the steady state was reached and the film stayed at the constant level of compression for some time before visible buckles appeared.

Finally, Fig. 11a plots the measured wrinkle wavelengths as a function of the strain rate for a single film length of $2L = 75$ mm, but at different liquid thicknesses. The chief trends evident in Fig. 11a are the increase in the wrinkle wavelength at large H_0 and at small compression rate. However, at small values of H_0, the wavelength becomes relatively insensitive to both of these parameters.

The end of Section 2.2 made a simple argument that the wavelength should scale as $\dot{\varepsilon}^{-0.5} {H_{s0}}^{0.5} {L_s}^{-1}$. These dependences were supported by the linear perturbation analysis (Fig. 6). Experimentally however, the wavelength dependence is weaker than expected. Fig. 11a shows that the curve with a $\dot{\varepsilon}^{-0.5}$ dependence is steeper than the measured data, especially at small H_0. The H_0 dependence of the wavelength is also weaker than expected. In the experiments, H_0 was increased from 0.9 mm to 2.5 mm, *i.e.* a factor of 2.7. If $\lambda \propto {H_{s0}}^{0.5}$, the wavelength should have increased by a factor of about 1.67. In fact, at any given compression rate, the wavelength is seen to increase by no more than a factor of 1.3. The prediction that $\lambda \propto {L_s}^{-1}$ is difficult to test with confidence due to the limited range of film lengths (65 mm to 80 mm) over which buckles are visible in our experiments.

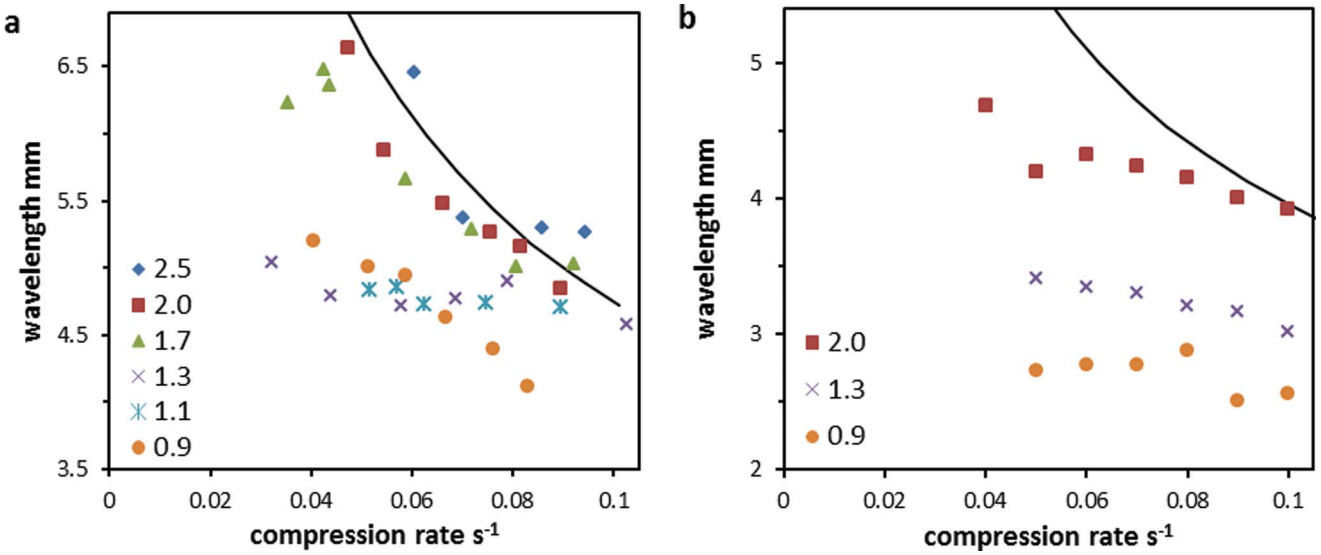

Fig. 11 (a) Experimentally-observed wavelength of wrinkles as a function of compression rate at the various liquid layer thicknesses (in mm) listed in the legend for film length of $2L = 75$ mm. (b) Wavelengths observed in analogous numerical simulations. Note the change in y-range. In both figures, the solid lines have a $\dot{\varepsilon}^{-0.5}$ dependence, but are not fits to any of the data.

One may also quantitatively compare the experimentally-observed wavelengths against predictions of the linear perturbation analysis. This comparison (online ESI Fig. S1†) shows that the observed wavelengths are typically twice of those predicted by linear perturbation analysis.

4.5. A critical view of the experiments

The chief critique of the experiments is that they cover only a limited parameter space. Most importantly, the experiments are all in the following regime: (1) $H_0 \gg h$, (2) $\lambda \sim H_0$, (3) the non-buckling region is a significant fraction of the film length, and (4) buckles appear at $t \gg \tau$. Whether the results would be qualitatively similar outside of this regime is not clear. A particularly interesting limit is when τ and σ_s^{max} are both large, *e.g.* because the film length, compression rate, or viscosity is large. In this case, the compressive stress builds up rapidly to a large value, and thus buckles are likely to appear at $t < \tau$. In the context of shear lag model, this limit offers considerable simplification since as per eqn (23), $\sigma_s = \dot{\varepsilon}t$, not just at the center, but over most of the film. Accordingly, all locations of the film except near the ends are expected to behave identically. However this limit also raises a potential complication: since σ_s grows with time in this regime, the fastest-growing wavelength changes continuously. In fact the dispersion relation is such that the longest wavelengths become unstable at the shortest times, but they grow slowly. In contrast, shorter wavelengths become unstable later, but they can grow much faster. Thus if a long wavelength mode starts with a large amplitude, it may become dominant simply because it becomes unstable earlier. Accordingly, the buckling process may become sensitive to long-wavelength imperfections.

Conducting experiments so that buckles appear at $t \ll \tau$ however is much more challenging. Changing most of the geometric or material properties is difficult: polymers with much higher viscosity at room temperature are available but they tend to be viscoelastic and furthermore take a much longer time to settle in the tray; increasing the film length much beyond the 75 mm used here would require far more careful handling to avoid damage before the film is deposited on the surface; using low modulus elastomeric films increases the difficulty of film handling since long films tend to stick to themselves because of static electricity; reducing H_0 greatly increases the time needed for the liquid to level itself in the tray. Thinner films are available but tend to have more defects. Indeed we have conducted experiments with polyester films of thickness down to 4.5 μm,[27] however these films had numerous small pre-existing wrinkles. In light of these limitations, the regime where buckles appear at $t < \tau$ is difficult to access. The most likelihood of success is by increasing the compression speed: our DC actuator offers a maximum speed of roughly 30 mm s^{-1}, whereas linear actuators with speeds of 500 mm s^{-1} are available. Such higher speeds may require some additional changes, *e.g.* the use of tension springs to guarantee that the rubber tray actually retracts at the imposed speed. Other potentially-fruitful approaches may be to reduce the viscosity (similar to our "hand experiments" of the Video M1.mpg†), while also reducing H_{s0} significantly.

We also note that large strain, viscous dominated experiments may also be conducted by entirely different sample-handling approaches. For instance one may readily prepare trilayer films (elastomer, glassy polymer, solid polymer) by coextrusion of plastics, or by spincoating polymers onto rubber sheets. The large strain retraction experiments may then be conducted at elevated temperatures at which the glassy polymer is molten, analogous to Fig. 1. However these experiments would likely suffer from complications such as fluid viscoelasticity, geometric imperfections, or non-isothermal effects, and likely not permit a "clean" comparison with theory. On the other

hand, these approaches would be valuable in materials science for developing surfaces with large amplitude textures.

5 Numerical simulations

The coupled differential equations for the in-plane and out-of-plane displacements, eqn (1) and (2), subject to the boundary conditions of eqn (3)–(6) were solved numerically (see online ESI†) following a method similar to Liang *et al.*[16] Fig. S2† shows the evolution of the displacement and stress in the film from the simulations using the same parameter values ($2L = 75$ mm, $h = 0.025$ mm, $H_0 = 0.9$ mm, $\dot{\varepsilon} = -0.088$ s^{-1}) as used in Fig. 3 and 8. The shear lag solution shows excellent agreement with the numerical simulation over most of the film except near the ends up to $t_s = 10\tau_s$. As the simulation continues, observable wrinkles appear after $t_s = 55\tau_s$, corresponding to about 0.3 s in dimensional time. Fig. S3† shows the growth of wrinkle amplitude and the simulated wrinkle profiles. The wrinkle profiles are comparable to the experiment in Fig. 8b–d, although the wrinkle amplitudes were not measured experimentally. Consistent with the experiments, the simulations show that wrinkles appear only when $t \gg \tau$, *i.e.* after the compressive stress in the film has reached the steady state. Fig. S3b† shows that even without any initial perturbation, wrinkling occurs near the center of the film with a specific, well-defined, wavelength. Limited simulations show that this buckling mode is insensitive to the initial perturbation: similar wrinkles are obtained with random initial perturbations of small amplitude. Interestingly, the growth of the wrinkle amplitude appears to follow a simple power law: $A \sim (t - t_c)^{0.5}$, as indicated by the solid line in Fig. S3a.† Finally we note from Fig. S3† that the ends of the film show an upward displacement, also consistent with experiments.

Numerical simulations were then conducted to test whether the experimental observations of Fig. 9 could be captured by the model. The results are summarized in Fig. S4,† which shows the film profiles under various conditions, all at the instant when the applied strain $\dot{\varepsilon}t = 0.06$. The effects of strain rate and film length noted experimentally are both well-captured by the simulations (Fig. S4a and b†): the wrinkle magnitude decreases with decreasing rate or film length until the wrinkles nearly disappear. However, Fig. S4c† shows that the effect of liquid thickness is not accurately reproduced: simulations show that the wrinkle amplitude increases with increasing H_0, in contradiction with experiments in Fig. 9c. This discrepancy is likely due to the lubrication approximation which assumes a thin viscous layer (*i.e.*, $H_0 \ll \lambda$) and becomes inaccurate for a relatively thick liquid layer. Indeed while the full analysis[14] shows that the growth rate plateaus for $H_{s0} > 10$, the lubrication analysis predicts an unbounded increase with H_{s0}. Thus for $H_{s0} > 10$, the lubrication approximation severely overestimates the wrinkle growth rate.

We then sought to identify the conditions under which wrinkles appear, *i.e.* a numerical analog of Fig. 10. Experimentally, the determination of whether wrinkles appear is made visually, as described in Section 4.4. Numerically, we apply an arbitrary criterion that wrinkles become visible if the amplitude exceeds 0.05 mm at the instant when $\dot{\varepsilon}t = 0.06$. This criterion allows calculating the minimum strain rate for wrinkling under given simulation conditions. These calculated values for $H_s = 0.9$ mm are plotted as open circles in Fig. 10. The simulations show reasonable agreement with experiment although it must be noted that the quality of agreement may improve or worsen if our arbitrary criterion (buckling amplitude of 0.05 mm) were to be changed. More importantly, the numerically-determined critical strain rate has a similar dependence on the film length as the scaling $\dot{\varepsilon} \propto L^{-4}$ (the straight line) predicted by the stress argument (eqn (19)).

Finally Fig. 11b quantifies the dependence of the wrinkle wavelength on the strain rate and the liquid layer thickness at a film length of $2L = 75$ mm. The qualitative trends are similar to experiments (Fig. 11a): the wavelength increases with decreasing rate, or with increasing liquid layer thickness. However, the wavelength values are typically 40% smaller than found experimentally, and furthermore, they show a weaker dependence on rate than experiment. Similar to the comments above, this discrepancy may be attributed to the assumption of a thin liquid layer in the lubrication approximation of the model.

6 Conclusion

In summary, this article shows that by using an elastomeric sheet as a "handle" and a viscous liquid as a supporting layer, an elastic film can be subjected to severe compression, and therefore wrinkles or high amplitude folds can be developed. This article focuses on the small-deformation regime. Dimensional analysis suggests that the buckling behavior is controlled by three non-dimensional parameters. Two of these parameters are geometric: the film length and the liquid layer thickness, both normalized by film thickness. The third is mechanical: the strain rate, normalized by a time scale proportional to the ratio of the liquid viscosity to the film modulus. This article develops a mechanical model which captures the coupling between the linear elastic deformation of the film and the viscous flow of the liquid layer under lubrication approximations. For the limiting case when out-of-plane displacements are negligible, a shear lag model is developed to predict evolution of compressive stress in the elastic film. An approximate linear perturbation analysis of this baseline solution predicts the rate at which perturbations at various wave numbers grow, and thus identifies the fastest growing mode. Numerical simulations of the full set of equations are also conducted which predict evolution of wrinkle amplitude and their wavelength. Experiments in one limiting regime (in which wrinkles appear after the compressive stress reaches the steady state) show that experimental trends are qualitatively consistent with these predictions. Quantitatively, the wavelengths measured experimentally are typically two-fold larger than those predicted by linear perturbation analysis, and ~40% larger than predicted by numerical simulations.

One motivation for this research was to develop a method to measure the mechanical properties of compatibilizer films[24–26] formed by a chemical reaction at the interface between immiscible homopolymers, or of other thin films such as

surfactant monolayers or graphene sheets in contact with viscous media.[28,29] Although a first step, this article is not a sufficient basis for such a method: a more accurate prediction of wave number, a validation in the short time limit discussed in Section 4.5, and a modified model that accounts for a thick viscous overlayer would be necessary before this approach can be used for thin film metrology. A second motivation was to develop a method of generating high aspect ratio features on surfaces. This paper already shows an example of how high amplitude wrinkles can be developed and quenched using a thermoplastic polymer as the substrate liquid (Fig. 1d–g). Further implementation of this idea would benefit from a clearer understanding of the post-buckling structural evolution, and in particular of how sinusoidal wrinkles evolve into sharp, localized folds. Particularly useful for this application is that using a rubber layer to support the liquid allows an additional level of control, *e.g.* by patterning the rubber so that buckles appear at programmed locations.

Acknowledgements

SC and SV were supported by the AFOSR (Natural Materials and Systems & Extremeophiles program) under award no. FA9550-10-1-0329, and by ACS-PRF grant no. 53386-ND7. CM acknowledges support from a NASA-PSGC scholarship award. PW and RH gratefully acknowledge financial support by the National Science Foundation through grant no. 1200161.

References

1 N. Bowden, S. Brittain, A. Evans, J. Hutchinson and G. M. Whitesides, *Nature*, 1998, **393**, 146–149.
2 M.-W. Moon, S. H. Lee, J.-Y. Sun, K. H. Oh, A. Vaziri and J. W. Hutchinson, *Proc. Natl. Acad. Sci. U. S. A.*, 2007, **104**, 1130–1133.
3 J. Huang, M. Juszkiewicz, W. H. de Jeu, E. Cerda, T. Emrick, N. Menon and T. P. Russell, *Science*, 2007, **317**, 650–653.
4 D. Vella, M. Adda-Bedia and E. Cerda, *Soft Matter*, 2010, **6**, 5778–5782.
5 E. Cerda, *J. Biomech.*, 2005, **38**, 1598–1603.
6 J. Y. Chung, A. J. Nolte and C. M. Stafford, *Adv. Mater.*, 2011, **23**, 349–368.
7 K. D. Hobart, F. J. Kub, M. Fatemi, M. E. Twigg, P. E. Thompson, T. S. Kuan and C. K. Inoki, *J. Electron. Mater.*, 2000, **29**, 897–900.
8 P. Yoo and H. Lee, *Macromolecules*, 2005, **38**, 2820–2831.
9 J. S. Sharp, D. Vader, J. a Forrest, M. I. Smith, M. Khomenko and K. Dalnoki-Veress, *Eur. Phys. J. E: Soft Matter Biol. Phys.*, 2006, **19**, 423–432.
10 J. R. Serrano, Q. Xu and D. G. Cahill, *J. Vac. Sci. Technol., A*, 2006, **24**, 324.
11 H. Jiang and J. Zhang, *J. Appl. Mech.*, 2008, **75**, 061019.
12 C. P. Brangwynne, F. C. MacKintosh, S. Kumar, N. a Geisse, J. Talbot, L. Mahadevan, K. K. Parker, D. E. Ingber and D. A. Weitz, *J. Cell Biol.*, 2006, **173**, 733–741.
13 R. Huang and Z. Suo, *J. Appl. Phys.*, 2002, **91**, 1135–1142.
14 R. Huang and Z. Suo, *Int. J. Solids Struct.*, 2002, **39**, 1791–1802.
15 N. Sridhar, D. J. Srolovitz and Z. Suo, *Appl. Phys. Lett.*, 2001, **78**, 2482.
16 J. Liang, R. Huang, H. Yin, J. Sturm, K. Hobart and Z. Suo, *Acta Mater.*, 2002, **50**, 2933–2944.
17 R. Huang, *J. Mech. Phys. Solids*, 2005, **53**, 63–89.
18 R. Huang and S. Im, *Phys. Rev. E: Stat., Nonlinear, Soft Matter Phys.*, 2006, **74**, 026214.
19 N. Mokni, M. Kostrzewa and F. Sidoroff, *Eur. J. Mech. Solid.*, 2008, **27**, 783–795.
20 L. Pocivavsek, R. Dellsy, A. Kern, S. Johnson, B. Lin, K. Y. C. Lee and E. Cerda, *Science*, 2008, **320**, 912–916.
21 H. Diamant and T. A. Witten, *Phys. Rev. Lett.*, 2011, **107**, 164302.
22 T. Wagner and D. Vella, *Phys. Rev. Lett.*, 2011, **107**, 044301.
23 D. Vella, J. Bico, A. Boudaoud, B. Roman and P. M. Reis, *Proc. Natl. Acad. Sci. U. S. A.*, 2009, **106**, 10901–10906.
24 P. Van Puyvelde, S. Velankar and P. Moldenaers, *Curr. Opin. Colloid Interface Sci.*, 2001, **6**, 457–463.
25 S. Dutta and D. J. Lohse, *Polymeric Compatibilizers*, Hanser Publications, Munich, 1996.
26 C. L. DeLeo and S. S. Velankar, *J. Rheol.*, 2008, **52**, 1385.
27 J. Niu, *Surface Wrinkling Based Method of Measuring Thin Film's Mechanical Properties*, M. S. Thesis, University of Pittsburgh, 2012.
28 J. Zasadzinski, J. Ding and H. Warriner, *Curr. Opin. Colloid Interface Sci.*, 2001, **6**, 506–513.
29 S. Stankovich, D. a. Dikin, R. D. Piner, K. a. Kohlhaas, A. Kleinhammes, Y. Jia, Y. Wu, S. T. Nguyen and R. S. Ruoff, *Carbon*, 2007, **45**, 1558–1565.

Online supplementary information

Governing Equations

For the viscous flow, we assume that the liquid thickness is small compared to the film length ($H_0 \ll L$), and by using the lubrication approximation we obtain:

$$\frac{\partial p}{\partial x} = \eta \frac{\partial^2 v_x}{\partial z^2} \tag{S1}$$

where p is the pressure in the liquid, v_x is the flow velocity in the x-direction, and η is the liquid viscosity; the effect of gravity as a body force is ignored. The viscous shear stress in the liquid is:

$$\tau_{zx} = \eta \frac{\partial v_x}{\partial z} \tag{S2}$$

At the top surface of the liquid layer ($z = H$) a shear stress is transferred to the elastic film:

$$T = \eta \frac{\partial v_x}{\partial z}\Big|_{z=H} \tag{S3}$$

At the bottom of the liquid layer, we assume no-slip at the liquid/rubber interface and hence have the boundary condition:

$$v_x = \dot{\varepsilon} x \text{ at } z = 0 \tag{S4}$$

where $\dot{\varepsilon}$ is the strain rate of the rubber contraction, with $\dot{\varepsilon} < 0$ for compression. The velocity is set to be zero at $x = 0$ (center of the film) to eliminate rigid-body motion.

Assuming the pressure p is independent of z for the thin liquid layer and integrating Eq. (S1) with the boundary conditions in Eqs. (S3) and (S4), we obtain:

$$v_x(z) = \frac{1}{2\eta}\frac{\partial p}{\partial x} z(z - 2H) + \frac{T}{\eta} z + \dot{\varepsilon} x \tag{S5}$$

The flow rate in the *x*-direction is then:

$$Q_x = \int_0^H v_x dz = -\frac{H^3}{3\eta}\frac{\partial p}{\partial x} + \frac{T}{\eta}\frac{H^2}{2} + \dot{\varepsilon} x H \tag{S6}$$

Using the mass conservation equation for an incompressible fluid:

$$\frac{\partial H}{\partial t} + \frac{\partial Q_x}{\partial x} = 0 \tag{S7}$$

The liquid thickness H is related to the out-of-plane displacement *w* of the top surface:

$$H(x) = H_0 + w(x) \tag{S8}$$

Substituting Eqs. (S6) and (S8) into Eq. (S7), we obtain an evolution equation

$$\frac{\partial w}{\partial t} = -\frac{\partial Q_x}{\partial x} = \frac{\partial}{\partial x}\left(\frac{H^3}{3\eta}\frac{\partial p}{\partial x} - \frac{H^2}{2\eta}T - \dot{\varepsilon}xH\right) \tag{S9}$$

and the in-plane displacement u of the top surface is related to the flow velocity in Eq. (S5) as

$$\frac{\partial u}{\partial t} = v_x|_{z=H} = -\frac{H^2}{2\eta}\frac{\partial p}{\partial x} + \frac{H}{\eta}T + \dot{\varepsilon}x \tag{S10}$$

For the elastic film, the equations are similar to Huang and Suo [13], except that there is no prestrain, but instead there are terms corresponding to the applied strain rate. The in-plane normal stress in the film is:

$$\sigma = \frac{E}{1-\nu^2}\left[\frac{\partial u}{\partial x} + \frac{1}{2}\left(\frac{\partial w}{\partial x}\right)^2\right] \tag{S11}$$

where E and ν are Young's modulus and Poisson's ratio of the elastic film, respectively. Subject to the viscous shear stress T across the film/liquid interface, force balance within the film requires that:

$$T = h\frac{\partial \sigma}{\partial x} \tag{S12}$$

In addition, a force balance perpendicular to the plane of the film yields:

$$p = D\frac{\partial^4 w}{\partial x^4} - \sigma h\frac{\partial^2 w}{\partial x^2} - T\frac{\partial w}{\partial x} \tag{S13}$$

Here D is the flexural rigidity of the elastic film: $D = \dfrac{Eh^3}{12(1-\nu^2)}$.

The boundary conditions to be applied at the ends of the film with $x = \pm L$ are:

No normal stress $$\frac{\partial u}{\partial x} + \frac{1}{2}\left(\frac{\partial w}{\partial x}\right)^2 = 0 \tag{S14}$$

No bending moment $$\frac{\partial^2 w}{\partial x^2} = 0 \tag{S15}$$

No shear force $$\frac{\partial^3 w}{\partial x^3} = 0 \tag{S16}$$

No pressure $$D\frac{\partial^4 w}{\partial x^4} - T\frac{\partial w}{\partial x} = 0 \tag{S17}$$

These are the same equations as Liang et al, (Acta Mater. **50**, 2933, 2002). The above equations can be non-dimensionalized by the scaled parameters as described in the main text, yielding the dimensionless evolution equations and boundary conditions given in the main text (Eqs. 1-6).

Linear Perturbation Analysis

Using Eqs. 20 and 21 in the main text as perturbations, the displacements can be written as a sum of the base (shear lag) solution and the perturbation:

$$w_s = w_s^{sh} + w_s^p \tag{S18}$$

and

$$u_s = u_s^{sh} + u_s^p \tag{S19}$$

where we denote the shear lag solutions with the superscript "sh". Substituting these values for u_s and w_s in the governing equations, subtracting the base equations i.e. the shear lag solutions (see main text), and neglecting nonlinear terms of the perturbation, we obtain the linear evolution equations for the displacement perturbations. The evolution for w_s can be written as:

$$\begin{aligned}\Omega_s B_0 = \Bigg[& \frac{1}{3} H_{s0}^3 \frac{\partial^2 p_s^p}{\partial x_s^2} - H_{s0} w_s^{sh} \left(\frac{1}{12} {k_s}^6 B_0 \right) + H_{s0}^2 \frac{\partial w_s^{sh}}{\partial x_s} \left(\frac{1}{12} i {k_s}^5 B_0 \right) \\ & - H_{s0} B_0 \frac{\partial^3 u_s^{sh}}{\partial x_s^3} - H_{s0} (i k_s B_0) \frac{\partial^2 u_s^{sh}}{\partial x_s^2} - \left(\frac{H_{s0}^2}{2} + H_{s0} w_s^{sh} \right) ({k_s}^3 A_0) + \left(H_{s0} \frac{\partial w_s^{sh}}{\partial x_s} \right) ({k_s}^2 i A_0) \\ & - \beta x_s (i k_s B_0) - \beta B_0 \Bigg]\end{aligned} \tag{S20}$$

Similarly, the corresponding evolution of the in-plane displacement can be written as:

$$\Omega_s A_0 = \left[i \frac{(H_{s0})^2}{2} \frac{\partial p_s^p}{\partial x_s} - H_{s0} w_s^{sh} \frac{{k_s}^5 B_0}{12} - H_{s0} ({k_s}^2 A_0) - w_s^{sh} ({k_s}^2 A_0) - i B_0 T_s^{sh} \right] \tag{S21}$$

In deriving these equations, terms containing $d\Omega_s/dt$ have been neglected, which is equivalent to assuming that the time-scale over which perturbations grow is very different from the time-scale over which the shear lag solution evolves.

The first derivative of pressure is written as:

$$\begin{aligned}\frac{\partial p_s^p}{\partial x_s} = & \frac{1}{12} i {k_s}^5 B_0 + N_s^{sh} (i {k_s}^3 B_0) + (k_s A_0) \frac{\partial^3 w_s^{sh}}{\partial x_s^3} + 2 T_s^{sh} ({k_s}^2 B_0) \\ & + 2 ({k_s}^2 i A_0) \frac{\partial^2 w_s^{sh}}{\partial x_s^2} - \frac{\partial T_s^{sh}}{\partial x_s} (i k_s B_0) - ({k_s}^3 A_0) \frac{\partial w_s^{sh}}{\partial x_s}\end{aligned} \tag{S22}$$

and the second derivative as:

$$\begin{aligned}\frac{\partial^2 p_s}{\partial x_s^2} = & -\frac{1}{12} {k_s}^6 B_0 - N_s^{sh} ({k_s}^4 B_0) + (k_s A_0) \frac{\partial^4 w_s^{sh}}{\partial x_s^4} + 3 T_s^{sh} (i {k_s}^3 B_0) + 3 (i {k_s}^2 A_0) \frac{\partial^3 w_s^{sh}}{\partial x_s^3} \\ & + 3 \frac{\partial T_s^{sh}}{\partial x_s} ({k_s}^2 B_0) - 3 ({k_s}^3 A_0) \frac{\partial^2 w_s^{sh}}{\partial x_s^2} - \frac{\partial^2 T_s^{sh}}{\partial x_s^2} (i k_s B_0) - ({k_s}^4 i A_0) \frac{\partial w_s^{sh}}{\partial x_s}\end{aligned} \tag{S23}$$

Thus Eqs. (S41) and (S42) can be represented as an eigenvalue problem of the form:

$$\Omega_s \begin{bmatrix} B_0 \\ A_0 \end{bmatrix} = \begin{bmatrix} M_{11} & M_{12} \\ M_{21} & M_{22} \end{bmatrix} \begin{bmatrix} B_0 \\ A_0 \end{bmatrix} \tag{S24}$$

where M_{11}, M_{12}, M_{21}, M_{22} are complex numbers, and functions of t_s and k_s.

The eigenvalues of the M matrix are the instantaneous growth rate Ω_s. The shear lag solution can be regarded as being unstable if the real part of the eigenvalue is positive. The eigenvalues were computed for various values of k_s using MATLAB (Mathworks Inc.). Of the two eigenvalues obtained from the equation, the one with the greater real part is considered as the dominant growth rate.

Quantitative comparison of linear perturbation analysis vs experiments

Figs. 7 and 11 in the main text respectively showed the fastest growing wavenumber predicted by linear perturbation analysis, and the wavelength observed experimentally. Fig. S1 compares them directly in non-dimensional form. The symbols are measured wavenumber at one specific liquid thickness, $H_0 = 0.9\ mm$ ($H_{s0} = 36$): filled points are same data as in Fig. 11a, whereas open points are two more experimental runs at the same liquid layer thickness. The solid line is a fit to the k_{sm} predicted by the linear perturbation analysis, i.e. it is the same as the solid line in Fig. 7a in the main text. In the experimental range, the linear perturbation analysis typically predicts the wavenumber to be roughly twice of what is observed experimentally.

Section 3 in the main text discussed the analogy between the situation at hand (film being compressed at a specified rate) and the situation where a film with a compressive prestrain ε_0 rests on a viscous liquid. Fig. 6 in the main text showed that the dispersion relation is similar in these two situations if the prestrain is assigned the value of the instantaneous strain. Here we will test this analogy against experiments taking advantage of the fact that in all our experiments, buckles appear at long times (i.e. $t \gg \tau$), when the scaled compressive stress has a value of σ_s^{max}. For the experimental value of $H_{s0} = 36$, it is reasonable to take the limit of an infinitely thick liquid layer considered by Sridhar et al (Appl. Phys. Lett. **78**, 2482, 2001). In that limit, the fastest-growing wave number is predicted to be $\sqrt{4\varepsilon_0(1+\nu)}$. Pursuing this analogy, we replace ε_0 with $|\sigma_s^{max}|$, thus giving the prediction that $k_{sm} = \sqrt{4\left(\frac{|\beta|L_s^2}{2H_{s0}}\right)(1+\nu)}$. This prediction, also plotted in Fig. S1, is up to 50% higher than the experiments.

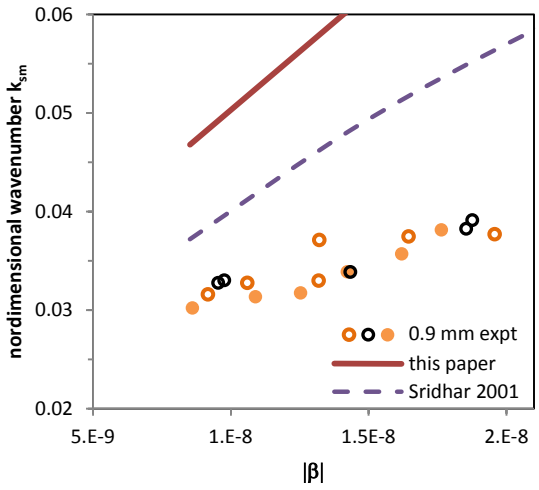

Fig. S1: Dimensionless wave number vs dimensionless compression rate. Solid symbols are the same as the 0.9 mm data in Fig. 11a in the main text. Open points are two more runs at the same liquid layer thickness. Solid line is a fit to the linear perturbation results, i.e. same as the solid line in Fig.7a in the main text. For explanation of dashed line, see above.

Numerical simulations

A numerical method based on a finite difference scheme was adopted, with center difference for space discretization and implicit backward difference for time integration. The method is similar to Liang et al. (Acta Mater. **50**, 2933, 2002), using fictitious nodes at each end to satisfy the boundary conditions. For each time step, the solution was obtained by iteration using the Newton-Raphson method.

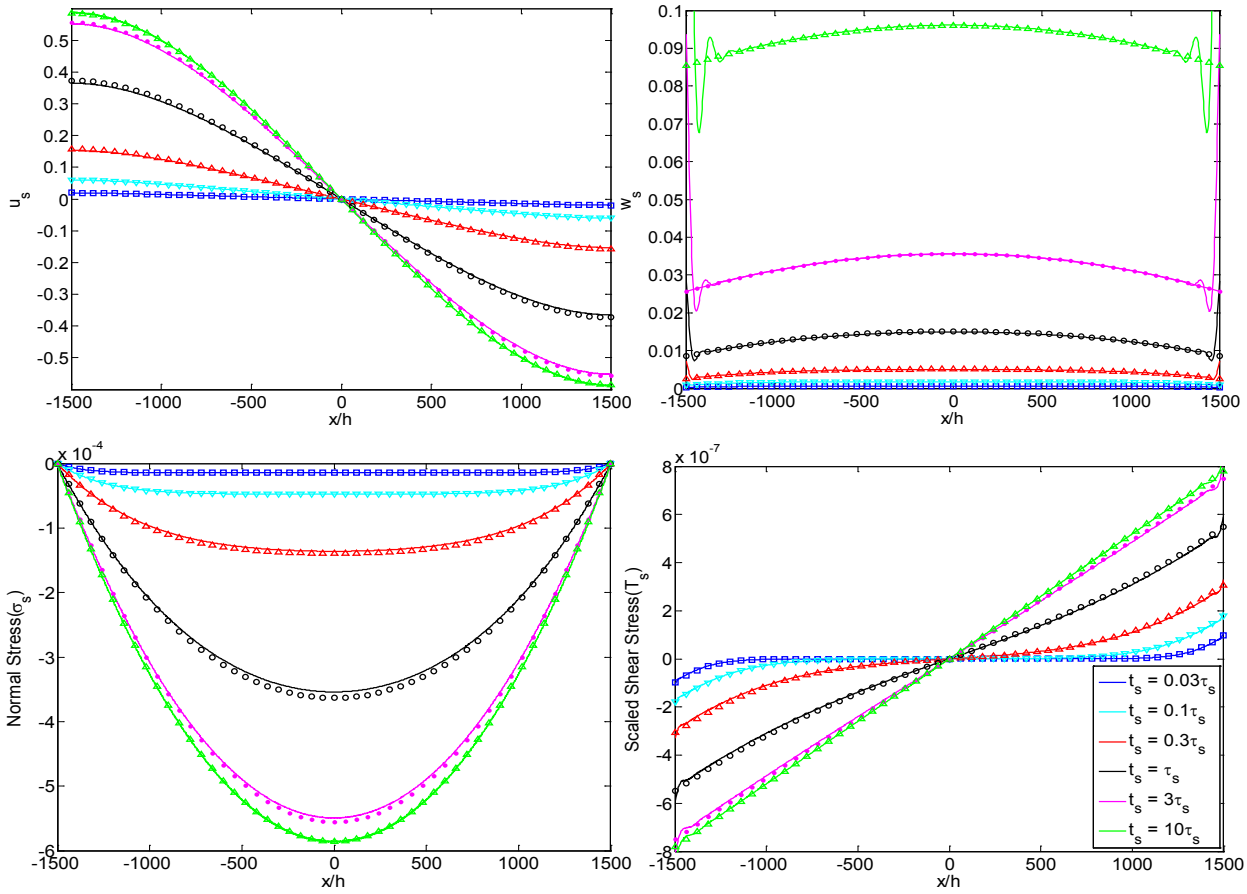

Fig. S2: Comparison of numerical simulation (solid lines) with the shear lag solution (symbols) at short times ($t_s \leq 10\tau_s$).

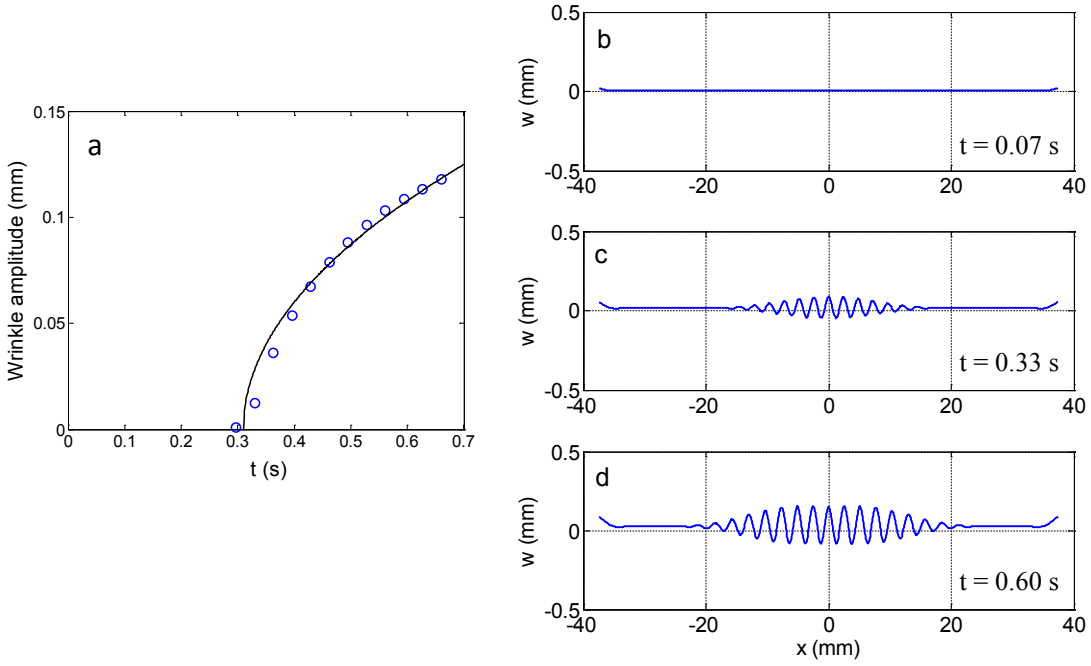

Fig. S3: Numerical simulation using the same parameters as the experiment of Fig. 8 in the main text ($2L$ = 75 mm; h = 25 μm; H_0 = 0.9 mm; $\dot{\varepsilon} = -0.088s^{-1}$). **a**. Evolution of wrinkle amplitude with time. The solid line indicates a simple power law: $A = k(t - t_c)^{0.5}$, with $t_c = 0.31s$. **b**-**d**. Simulated wrinkle profiles at various times, corresponding to Fig. 8b-d.

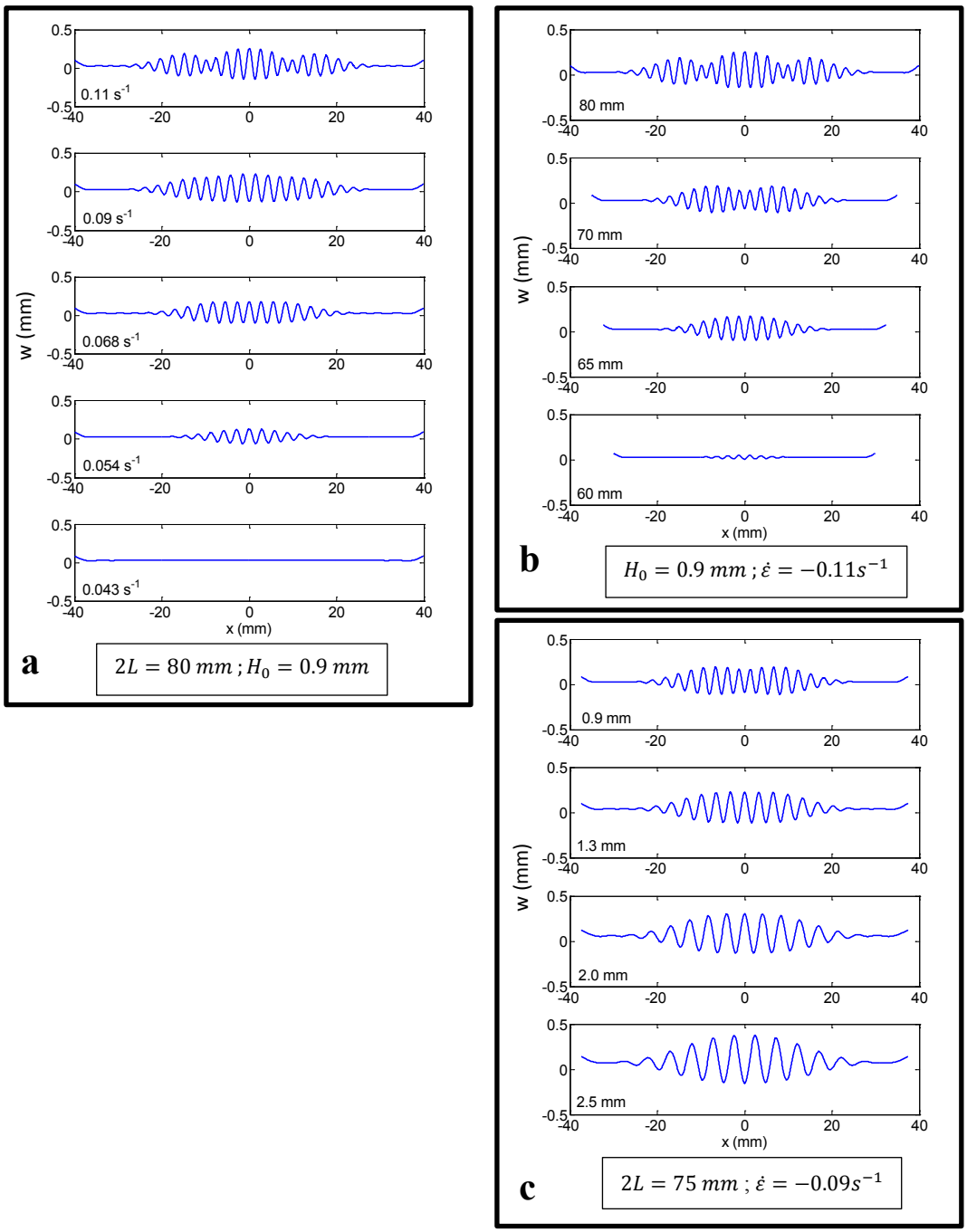

Fig. S4: Simulations approximately matching the conditions in the three panels in Fig. 9 in the main text, showing the effect of each of the three parameters on wrinkling. In all graphs, the y-axis is the dimensional value (in mm) of the out-of-plane displacement. Each graph corresponds to $\dot{\varepsilon}t = 0.06$.